POLITECNICO DI TORINO
Repository ISTITUZIONALE

DLP 4D-Printing of Remotely, Modularly, and Selectively Controllable Shape Memory Polymer Nanocomposites Embedding Carbon Nanotubes

Original
DLP 4D-Printing of Remotely, Modularly, and Selectively Controllable Shape Memory Polymer Nanocomposites Embedding Carbon Nanotubes / Cortes, A., Cosola, A., Sangermano, M., Campo, M., Gonzalez Prolongo, S., Pirri, C.F., Jimenez-Suarez, A., Chiappone, A.. - In: ADVANCED FUNCTIONAL MATERIALS. - ISSN 1616-301X. - ELETTRONICO. - (2021), p. 2106774. [10.1002/adfm.202106774]

Availability:
This version is available at: 11583/2934858 since: 2021-11-02T14:28:54Z

Publisher:
John Wiley and Sons Inc

Published
DOI:10.1002/adfm.202106774

Terms of use:

This article is made available under terms and conditions as specified in the corresponding bibliographic description in the repository

Publisher copyright

(Article begins on next page)

18 November 2026

Check for updates

ADVANCED FUNCTIONAL MATERIALS
www.afm-journal.de

DLP 4D-Printing of Remotely, Modularly, and Selectively Controllable Shape Memory Polymer Nanocomposites Embedding Carbon Nanotubes

Alejandro Cortés, Andrea Cosola, Marco Sangermano, Mónica Campo, Silvia González Prolongo, Candido Fabrizio Pirri, Alberto Jiménez-Suárez, and Annalisa Chiappone**

An in-depth investigation on novel electro-activated shape memory polymer composites (SMPCs) for digital light processing 3D-Printing, consisting of a poly(ethylene glycol) diacrylate/poly(hydroxyethyl methacrylate) matrix embedding multi-walled carbon nanotubes (CNTs), is reported here. The composition of the photocurable (meth)acrylate system is finely tuned to tailor the thermomechanical properties of the matrix, whereas the effect of CNTs on the photoreactivity and rheological properties of the formulations is investigated to assess the printability. Electrical measurements confirmed that the incorporation of CNT into the polymeric matrix enables the electrical conductivity and thus the possibility to remotely heat the nanocomposite using the Joule effect. The feasibility to drive a shape memory cycle via Joule heating is proved, given that the high shape fixity (R_f) and shape recovery (R_r) ratios achieved ($R_f \approx 100\%$, $R_r > 95\%$) confirmed the significant electrically-triggered responsiveness of such CNT/SMPCs. Finally, it is shown how to activate a modular and selective electro-activated shape recovery, which may ultimately envisage the 4D-Printing of remotely and selectively controllable smart devices.

1. Introduction

4D-Printing[1] has recently emerged as an exciting evolution of conventional 3D-Printing since it enables the fabrication of smart structures that can easily change their shape over time in response to a specific stimulus.[2–4]

Among all stimuli-responsive materials, shape memory polymers (SMPs) are of particular interest, given their ability to fix a temporary shape (TS) and return to their permanent shape (PS) once exposed to an external trigger,[5,6] such as water,[7,8] light,[9] pH variation,[10] and in particular, heat, which remains the most widely investigated triggering mechanism.[2,11–13]

Heat-activated SMPs require a transition temperature (T_{trans}), either a melting temperature (T_m) or a glass transition temperature (T_g), to govern a molecular switching phase that fix the TS, while crosslinking net-points are needed to both impart mechanical stability to the PS and drive the recovery. In particular, thermoresponsive SMPs are deformed when heated at $T > T_{trans}$ and the strained TS is fixed by subsequent rapid cooling at $T < T_{trans}$. Finally, the PS is recovered by reheating at $T > T_{trans}$ under stress-free conditions.[11,14,15]

However, direct heating entails some disadvantages, namely 1) low recovery rate due to low thermal conductivity of polymers and 2) impossibility to enable a remote control of the recovery. To remedy these issues, increasing attention has been given in the last few years to the study of electro-activated shape memory polymer composites (SMPCs), being these materials particularly promising for broadening the application fields of 4D-Printing, especially wherever direct heating is not possible. Indeed, the incorporation of a conductive filler in a SMP matrix allows to trigger the shape memory behavior via Joule heating, which implies a more homogeneous heat distribution (i.e., lower recovery times) and the feasibility of a fast, remote and selective control of the recovery.[5,16–20] In other words, selective shape memory can ultimately enable a multi-route shape recovery, being able to apply the proper stimuli just in the desired area, envisaging the possibility to design selectively controlled smart devices. In this regard, Shao et al.[21] prepared a biomimetic flower-shaped gripper where each petal could be remotely and selectively controlled by applying a voltage on electrically conductive hinges doped with silver nanowires to enable a shape memory effect driven by Joule heating.

A. Cortés, M. Campo, S. González Prolongo, A. Jiménez-Suárez
Materials Science and Engineering Area
Rey Juan Carlos University
C/Tulipán s/n, Móstoles, Madrid 28933, Spain
E-mail: alberto.jimenez.suarez@urjc.es
A. Cosola, M. Sangermano, C. F. Pirri, A. Chiappone
Department of Applied Science and Technology
Politecnico di Torino
Corso Duca degli Abruzzi 24, Torino 10129, Italy
E-mail: annalisa.chiappone@polito.it

The ORCID identification number(s) for the author(s) of this article can be found under https://doi.org/10.1002/adfm.202106774.

© 2021 The Authors. Advanced Functional Materials published by Wiley-VCH GmbH. This is an open access article under the terms of the Creative Commons Attribution License, which permits use, distribution and reproduction in any medium, provided the original work is properly cited.

DOI: 10.1002/adfm.202106774

Despite metal particles provide excellent electrical and thermal conductivity,[22,23] they are expensive, easy to oxidize, and high concentrations are needed to reach the percolation threshold. Conversely, carbon-based materials (e.g., carbon black, carbon nanotubes (CNTs), carbon nanofibers, and graphene) provide excellent mechanical properties and electrical conductivity at much lower concentrations due to their outstanding specific surface area and aspect ratio, which makes them the most attractive fillers for the development of conductive SMPCs.[16,24]

The fabrication of electro-activated SMPCs embedding carbon-based fillers have been explored by means of different 3D-Printing technologies,[25] ranging from Spray Deposition Modeling,[26] solvent-cast 3D-Printing,[27] Direct Ink Writing (DIW)[28,29] to Fused Deposition Modeling (FDM).[17,30–32] Nevertheless, just one study has been found on 3D printed selectively electro-activated SMPCs embedding carbon-based fillers.[17]

Whereas, the use of those 3D-printing technologies commonly known as vat polymerization techniques (Stereolithography, SLA; Digital Light Processing, DLP) that exploit a photochemical process to convert a photocurable liquid resin into a solid with an extremely high level of resolution, remains a challenge. Zarek et al. prepared electro-activated SMPs via DLP-printing but here CNTs are just deposited via subsequent Inkjet printing and not incorporated in the photocurable resin,[11] while, to date, just one work has been reported on CNT/SMPCs prepared directly by DLP 3D-Printing (Mu et al.).[33] In this regard, the lack of photocurable SMP, the high viscosity of the doped formulations, and the light scattering induced by the filler are the main limitations to the fabrication of SMPCs via SLA/DLP processes.[25]

Trying to fill this gap, we report in this study the development of novel electro-activated SMPCs consisting of a photocurable and DLP printable SMP matrix embedding multi-walled CNTs. The optimization of the formulation and the study of its printability, together with the analysis of the electro-thermal properties of the material, enabled the preparation of electrically controllable DLP printed SMPCs. A multi-material object was prepared as a proof of concept, to show the potential integration of such SMPCs for the fabrication of smart electro-activated structures. Finally, the possibility to drive via Joule heating both a modular recovery, being able to stop and resume it when desired, and a selective actuation were demonstrated. As far as we know, this is the first in-depth investigation on remotely, modularly, and selectively controlled electrically-triggered SMPCs prepared by DLP 3D-Printing.

2. Results and Discussion

2.1. Optimization and Characterization of the Photocurable System

The aim of this work was to prepare DLP-printable electro-activated SMPCs. Being known the excellent thermally-triggered shape memory properties of hydrogen-bonding stabilized polyhydroxyethylmethacrylate (PHEMA) thermosets (shape fixity and shape recovery close to 99%),[34] the followed strategy was to use HEMA as the main component of an amorphous thermosetting matrix wherein poly(ethyleneglycol)diacrylate (PEGDA, Mn = 700 g mol^{-1}) serves as a crosslinking agent. Electrically conductive CNTs were incorporated to enable the shape recovery via Joule heating, while phenylbis(2,4,6-trimethylbenzoyl)phosphine oxide (BAPO) was used as a photoinitiator.

First, the composition of the (meth)acrylate photocurable system was finely tuned, aimed to design a SMP matrix with 1) a mild T_g to both minimize the voltage required to activate the recovery via Joule heating and to store a mechanically stable temporary-strained configuration at room temperature (RT, around 25 °C) and 2) a high elasticity ratio (E_g/E_r, where E_g and E_r are the glassy and rubbery modulus, respectively), preferably around two orders of magnitude, to guarantee both an acceptable stretchability during the programming stage at $T > T_g$ and good resistance to deformation at $T < T_g$.[35–37]

Preliminary DMTA measurements revealed that thermosets with highly tunable thermomechanical properties can be prepared by simply adjusting the PEGDA:HEMA ratio in the neat precursor formulation. As can be seen in **Figure 1**, the T_g gradually increases as the HEMA content is increased in the precursor formulation, ranging from −30 (pure PEGDA) to 120 °C (PEGDA:HEMA = 1:50). As already reported in the literature,[38,39] the glass transition temperature of a polymer increases linearly with the concentration of hydrogen bonding groups, given that the mobility of the polymeric chains' results restricted in the presence of an H-bonded supramolecular network. The trend observed in the DMTA plots is consistent with these findings since the increase in the T_g may be related to the ever-higher density of H-bonds when increasing HEMA content.[34] Moreover, as the content of PEGDA decreases, E_r decreases from 23 to 0.045 MPa due to a lower crosslinking density,[40] thus giving higher elasticity ratios.

Based on these data, keeping the PEGDA:HEMA weight ratio at 1:3 allows to prepare mechanically stable thermosets that fulfill all the above-mentioned prerequisites, namely 1) a T_g of 70 °C that can ultimately enable to fix a temporary-strained shape at RT and 2) a high drop in the storage modulus (E′) in

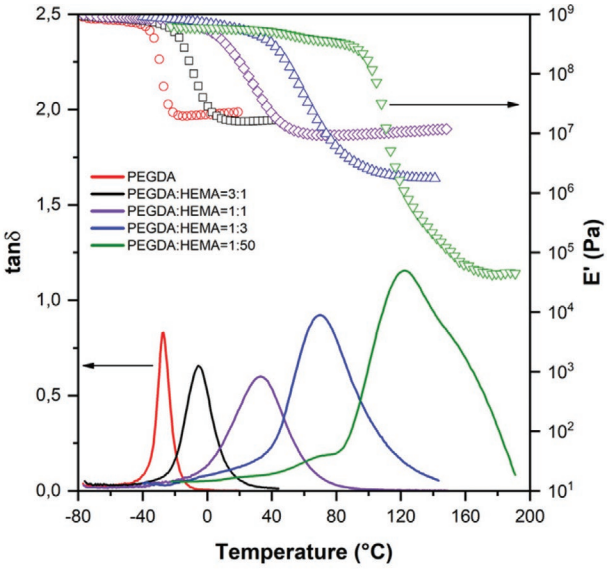


Figure 1. DMTA plots of DLP-printed PEGDA-*co*-PHEMA thermosets prepared by varying the PEGDA:HEMA ratio in the precursor formulations, while BAPO was used as a photoinitiator in 1 wt.%.

© 2021 The Authors. Advanced Functional Materials published by Wiley-VCH GmbH

Table 1. Composition of the final photocurable formulations and viscosity values calculated at a shear rate of 1 s^{-1}.

Formulation	PEGDA:HEMA [wt./wt.]	BAPO [wt.%]	CNTs [wt.%]	H [Pa s]
F0	1:3	1	–	0.01
F0.1	1:3	1	0.1	0.73
F0.3	1:3	1	0.3	0.89
F0.5	1:3	1	0.5	11.69

the T_g region (E_r of 1.7 MPa, and E_g/E_r of 5.4×10^2) which can guarantee large elastic deformation during the programming phase. Instead, the PEGDA-*co*-PHEMA polymers prepared with lower content of HEMA (higher PEGDA:HEMA ratio) are not suitable for our purposes, since their low T_g would make the programming of the fixing stage at RT impossible. Whereas, it is preferable not to lower the PEGDA:HEMA ratio since increasing content of HEMA would lead to ever-higher T_g and, therefore, to the need for applying an ever-higher voltage to enable the shape recovery by means of Joule heating. Likewise, a decrease of PEGDA content would imply a lower shape recovery rate, as already reported when reducing the crosslinking density of an SMP.[41–43]

Accordingly, doped photocurable formulations were prepared by dispersing different amounts of CNTs (0.1, 0.3, and 0.5 wt.%) in the acrylic monomers, while keeping fixed both the PEGDA:HEMA weight ratio at 1:3 and the concentration of the BAPO photoinitiator at 1 wt.% (see **Table 1**).

Prior to 3D-Printing, the effect of the CNTs on the viscosity and the photopolymerization kinetics was assessed, being these parameters significantly relevant for a DLP process.

Unlike the neat formulation (F0), all the doped formulations (referred to as FX, where X is the concentration of CNTs in wt.%) show a typical shear-thinning behavior (Figure S1, Supporting Information), in good accordance with previous reports on resins embedding nanofillers.[44,45] Further, as becomes clear from the values reported in Table 1, the higher the content of CNTs, the higher the viscosity of the formulations since the interaction between the CNTs limits the mobility of the polymer chains. However, according to the literature, such viscosity values are acceptable for DLP-Printing.[44]

Then, the photopolymerization kinetics was evaluated via real-time photorheology, monitoring the evolution of the storage modulus (G') during UV-light irradiation. The photorheology plots given in **Figure 2**a revealed the high reactivity of all the formulations, confirming their suitability for a DLP 3D-Printing process. However, the presence of CNTs led to a delay of the onset of photopolymerization and to slower kinetics, as evidenced by the decreased slopes of the G' curves, suggesting the need for longer exposure times during 3D-Printing. In particular, the delay time (i.e., the time needed to observe the increase of G' modulus after switching on the light) increases from 10 s up to 19 s by increasing the CNT content in the precursor formulation, while the curing rate ($\Delta G'/\Delta t$) is slowed down from 9 to 2 kPa s^{-1} (Figure 2b).

The lower photo-reactivity can be ascribed to the UV shielding effect of CNTs, whose light absorption can clash with the initiating efficiency of the photoinitiator, resulting in a delayed and slowed photopolymerization.[44,46] Moreover, the higher G' values of the doped formulations before the onset of photo-crosslinking are consistent with the observed increase of the viscosity of the formulations.

In order to avoid both over UV-shielding and further viscosity increases, which would result into undesired DLP-processing issues, such as adhesion forces between the vat and the building platform while printing, higher CNT contents have not been considered for further investigations.

2.2. DLP 3D-Printing and Characterization of the CNT Nanocomposites

Once the photo-reactivity has been assessed, the printability of all the formulations was proved, since computer-aided design (CAD) models were successfully reproduced using a commercial DLP-printer, starting from simple flat samples to more complex ones such as the honeycomb-like structure shown in **Figure 3**a. According to the photorheology data, the printing parameters

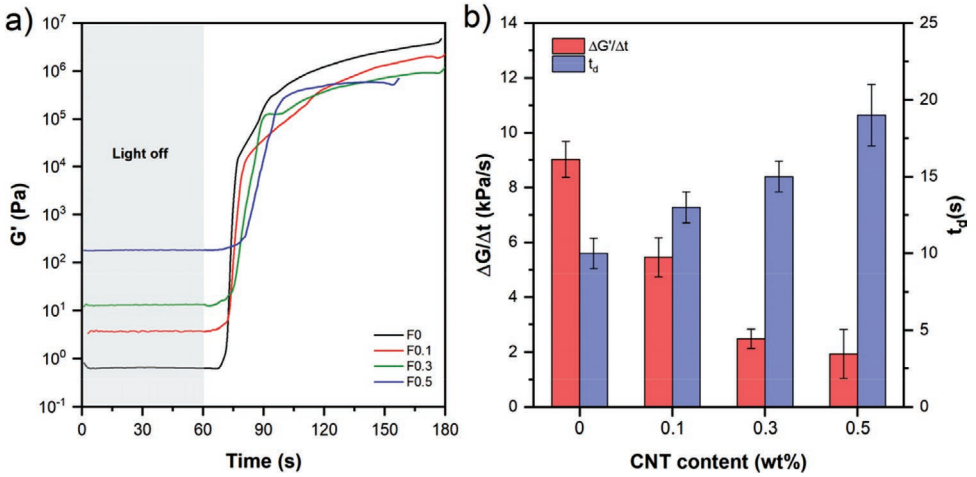


Figure 2. a) Photorheology plots corresponding to the evolution of the storage modulus (G') of both the neat (F0) and doped formulations (F0.1, F0.3, and F0.5) during UV-light irradiation (light switched on after 60 s); b) measured kinetic data (delay time, t_d, and curing rate, $\Delta G'/\Delta t$) as a function of the CNT content.

© 2021 The Authors. Advanced Functional Materials published by Wiley-VCH GmbH

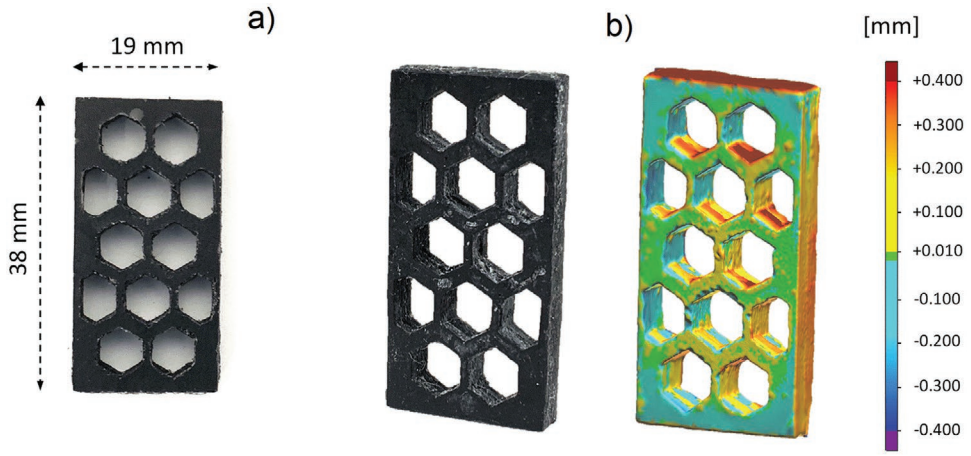


Figure 3. a) 3D-printed honeycomb-like structure and b) heat-map obtained by 3D scanning representing the fidelity of the printed structure to the digital CAD model.

have been specifically optimized for each precursor formulation, setting longer exposure times as higher the content of CNTs is (from 7 s/layer for F0 to 24 s/layer for F0.5). To confirm the effective formation of crosslinked polymers during the printing process, the gel content (GC) was evaluated. High GC values were observed for all the samples (GC above 90% for all the specimens) with a limited decrease of the insoluble fraction at the increase of the CNTs content (**Table 2**) that may be ascribed to the UV-light shielding effect induced by the filler.[44,46]

Afterwards, the resolution of the printed parts was evaluated by means of 3D scanning. First, the structure is digitalized via a 3D inspection and then overlaid to the original digital CAD file. Finally, the results of the comparative analysis are displayed as a colored 3D map showing the geometrical deviation from the reference model, where the red zones represent the "material-excess" and the blue ones correspond to areas with a "material-deficit".[47,48] From the final comparison of the data (Figure 3b), the deviation between positive and negative displacements of the 3D-Printed part from the CAD file was found to be ±0.16 mm.

Flat printed samples were used to preform DMTA analyses aiming to evaluate the thermal and viscoelastic properties of the nanocomposites. As summarized in Table 2, no significant trend in the T_g was observed when increasing the nanofiller content (see Figure S2, Supporting Information). This may be explained by assuming two competitive effects: on the one hand a stiffening of the thermosets induced by the presence of the carbon filler which hinders the mobility of the polymeric chains, as reported for polymeric composites embedding CNTs,[46,49] on the other hand a flexibilization of the network due to the reduction of the crosslinking density induced by the UV-shielding effect of CNTs. However, the resulting glass transition temperatures (ranging from 62 to 81 °C) would easily allow to fulfill the prerequisite of fixing a temporary-strained shape at RT.

Table 2. Properties of the thermosetting nanocomposites prepared by DLP-printing (Samples denoted as SX, where X is the amount of CNTs).

Sample	GC [%]	T_g [°C]
S0	99.3 ± 0.3	70
S0.1	96.1 ± 1.4	62
S0.3	95.0 ± 2.6	72
S0.5	90.5 ± 0.7	81

Electrical and electro-thermal characterizations were then performed on the DLP-printed nanocomposites to evaluate 1) the content of filler to enable the electrical conductivity and 2) the minimum voltage to reach the T_g by Joule heating, to prove the possibility to perform a shape memory cycle by simply exploiting the heat release while applying a voltage.[20] Copper electrodes were placed at opposite ends of the longest dimension of the specimens using a silver paste to reduce the electrical resistance.

The evolution of electrical conductivity (σ) as a function of the CNT content is shown in **Figure 4**a. According to these data, the electrical percolation threshold, taken as the critical content of conductive filler needed to get a significant increase in the electrical conductivity,[50] was found to be around 0.1 wt.% CNTs. The further increase in σ from 5.4×10^{-4} S cm^{-1} (S0.1) up to a plateau value of 5.8×10^{-1} S cm^{-1} reached with 0.5 wt.% of CNTs (S0.5), can be ascribed to the increased volume fraction of the nanofiller in the polymeric matrix.[51]

As well established, polymers embedding conductive fillers can be internally heated by simply applying a voltage.[20] Indeed, an increase in electrical conductivity leads to increased current intensity, and therefore to an increased heat development due to the higher release of Joule energy according to Joule's law.

In this regard, the average temperature increment (ΔT_{av}, relative to RT) of the nanocomposite specimens as a function of both the applied voltage and the CNT content are given in Figure 4b. As expected, ΔT_{av} increases as the CNT content increases and the temperature distribution looks rather homogeneous (Figure 4c), indicating a relatively good dispersion of the CNTs, in accordance with previous studies.[52] In this regard, the voltage needed to reach a T_{av} equal to the T_g is around 160 V for S0.5 (0.5 wt.% CNT) and 250 V for S0.3 (0.3 wt.% CNT). Remarkably, no temperature increase was noted for S0.1 (0.1 wt.% CNT). This may be explained by assuming that the electrical conductivity of the latest sample is not enough to enable the Joule heating, at least by applying up to 300 V.

© 2021 The Authors. Advanced Functional Materials published by Wiley-VCH GmbH

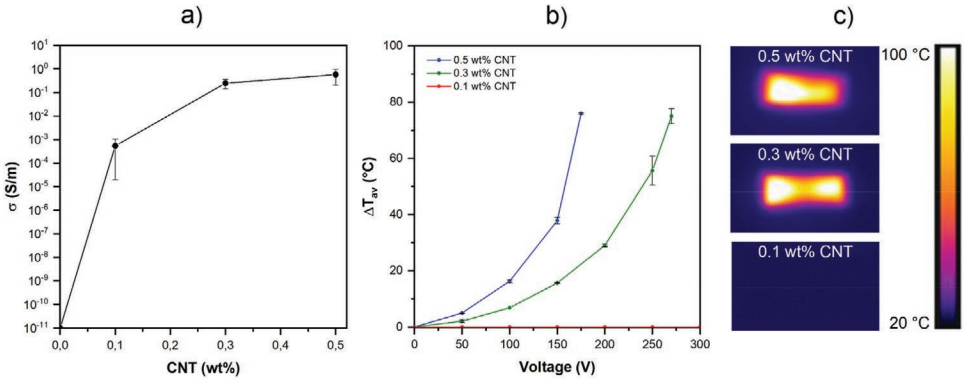


Figure 4. a) Electrical conductivity as a function of CNT content; b) ΔT_{av} reached by Joule heating (calculated with regard to RT) as a function of both the applied voltage and the CNT content; and c) images taken from the thermal camera showing the temperature distribution in the printed nanocomposites as a result of the heat release at 170 V for S0.5 (0.5 wt.% CNT), 270 V for S0.3 (0.3 wt.% CNT), and 300 V for S0.1 (0.1 wt.% CNT).

2.3. Shape Memory Behavior Activated by Joule Heating

In the case of SMPs, the integration of conductive fillers may ultimately enable an electrically-triggered shape memory effect driven by internal heating.[20] Therefore, the Joule heating stimulated shape memory behavior of the nanocomposites was investigated.

In particular, the programming step was carried out by applying to a DLP-printed sample ($30 \times 10 \times 2$ mm^3), the voltage needed to increase its temperature at $T = T_g + 20$ °C. Once the deforming temperature has been reached, the sample is bent by using a U-shaped mold (**Figure 5**a, Figure S3, Supporting Information) and the TS is fixed by cooling at RT under fixed strain conditions. After holding the TS at RT for 5 min, the sample is finally reheated at $T = T_g + 20$ °C by applying the same voltage used for the deforming stage and the PS is recovered.

Based on the electrothermal characterization, the voltage needed to reach a T_{av} equal to $T_g + 20$ °C is around 170 V for S0.5 and 270 V for S0.3. The specimen with the lowest content on CNT (S0.1) was not used for the shape memory tests activated by Joule heating, given that no temperature increase was noted by increasing the voltage, as previously discussed. The capability of the material to both maintain the applied strain (shape fixity ratio, R_f) and recover the original configuration (shape recovery ratio, R_r), as well as the recovery time (t_r), were evaluated. As a way of comparison, the shape memory parameters R_f, R_r, and t_r were also monitored by performing a shape memory cycle triggered by conventional direct heating (Figure 5b).

The results of the shape memory characterization as a function of both CNT content and triggering method (either direct or Joule heating), are reported in **Table 3**. All the specimens present an R_f near 100% independently from the heating source used for the shape memory cycle, confirming the high stability of the strained configuration at RT after unloading. In this regard, the shape fixity is fostered by means of hydrogen bonds recombination. As previously reported, the H-bonds occurring

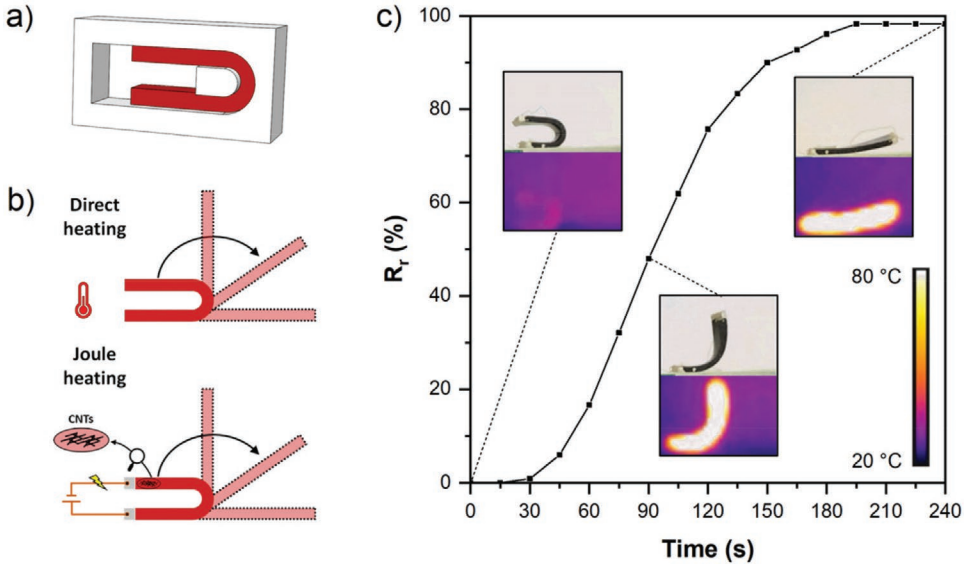


Figure 5. a) DLP-printed mold used to program the TS; b) two strategies followed to trigger the shape recovery (direct heating and Joule heating); and c) evolution of the Joule heating triggered shape recovery of S0.5 over time followed with the thermal camera.

© 2021 The Authors. Advanced Functional Materials published by Wiley-VCH GmbH

Table 3. Results of the shape memory characterization of the DLP-printed nanocomposites.

Sample	CNT [wt.%]	Direct heating			Joule heating		
		R_f [%]	R_r [%]	t_r [min]	R_f [%]	R_r [%]	t_r [min]
S0	–	≈ 100.0	99.1	7.7	–	–	–
S0.1	0.1	≈ 100.0	99.3	5.4	–	–	–
S0.3	0.3	≈ 100.0	98.3	5.5	≈ 100.0	98.7	3.4
S0.5	0.5	≈ 100.0	95.3	6.2	≈ 100.0	96.7	3.6

via the side terminal -OH groups of HEMA, which were broken during the deforming stage while heating at $T = T_g + 20$ °C, can reassociate at RT, thus stabilizing the TS.[34]

The high R_r ratios (>95%) proved that the DLP-printed nanocomposites can easily recover their PS from a mechanical deformation. The shape recovery evolution triggered by Joule heating of a nanocomposite specimen over time is given in Figure 5c. However, a slight decrease in R_r was observed with increasing CNT content. This can be explained by the generation of CNT aggregates with increasing filler content, which hinders a complete recovery by limiting the mobility of the polymeric chains.[53]

Remarkably, the higher R_r and shorter t_r needed by following the Joule heating route revealed the higher efficiency of the electrically activated shape recovery over the one triggered by the conventional direct heating. This can be ascribed to a more uniform thermal distribution due to the intrinsic volumetric heating obtained by the Joule effect, whereas direct heating strongly depends on the thermal conductivity of the specimen since is conducted from the surface to the inner region. In this sense, Joule heating is generally considered one of the most effective ways to provide uniform heating of electrically conductive composite materials.[54–56]

Given the similar electrically-activated shape memory response of the nanocomposite specimens S0.3 and S0.5 in terms of R_f, R_r, and t_r, but the much lower voltage needed to reach the T_g by increasing the filler content, 0.5 wt.% was selected as the optimum CNT content for further shape memory investigations.

First, we evaluate the potential integration of these SMP nanocomposites in the fabrication of a smart multimaterial structure by means of DLP-printing. For this purpose, a butterfly-shaped 3D-structure was suitably designed (**Figure 6**a) with a nanocomposite part (see component 2, prepared from S0.5) to enable a shape memory behavior triggered by Joule heating. Commercial PEGDA (Mn = 250 g mol^{-1}) was used to prepare the remaining non-conductive portion of the butterfly body and the wings (component 1, for more details on the formulations, see Table S1, Supporting Information). The multimaterial structure was obtained by simply changing the resin vat while printing. Then, the electrodes were placed behind the wings (components 3–4).

Once again, the TS was programmed with a deforming stage at $T = T_g + 20$ °C followed by rapid cooling at RT under fixed strain conditions. The recovery was carried out by reheating at $T = T_g + 20$ °C and monitored by following the reopening of the butterfly wings (Figure 6b) over time. A lower voltage was

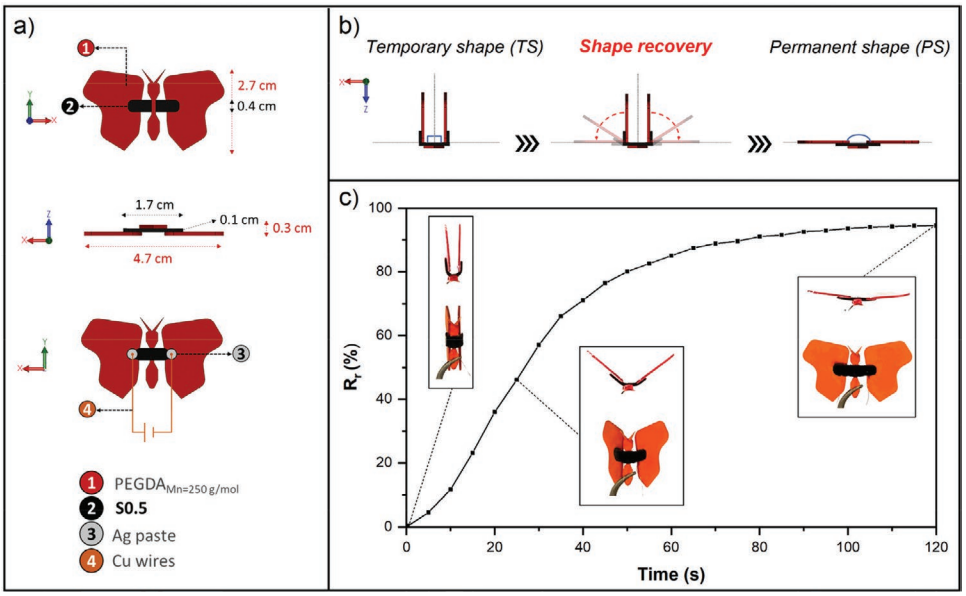


Figure 6. a) CAD model of the butterfly-shaped smart structure; b) schematic representation of the shape recovery; and c) recovery of the PS over time, upon the application of a voltage of 80 V.

© 2021 The Authors. Advanced Functional Materials published by Wiley-VCH GmbH

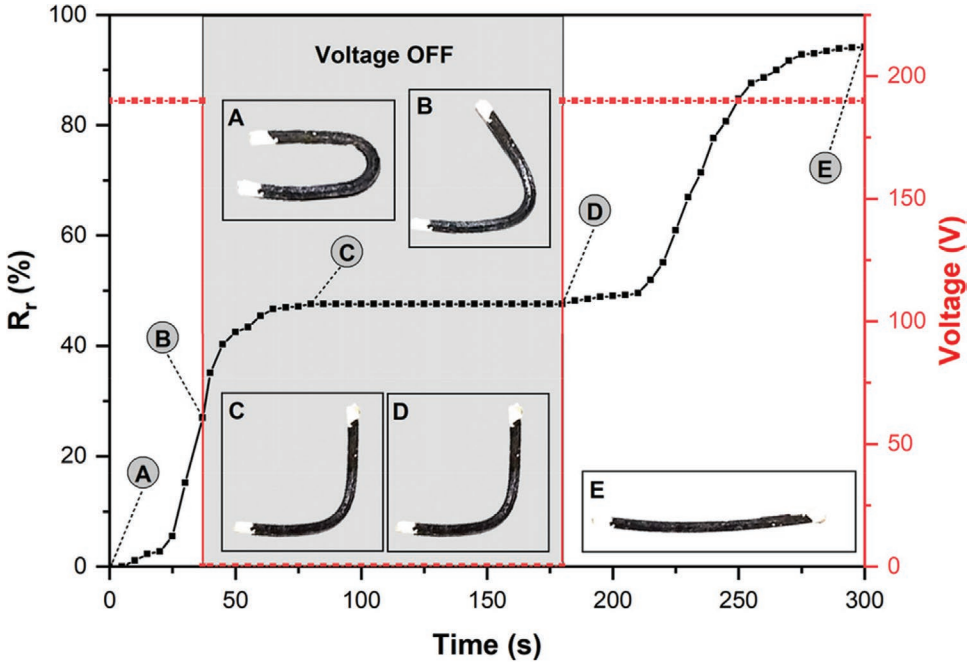


Figure 7. Modular recovery of the PS driven by simply turning on and off the voltage as a function of time.

needed (80 V) to increase the T up to T_g + 20 °C with regard to the previous investigations on S0.5 (170 V, see Figure 4b), due to the lower electrical resistance resulting from both the different geometry of component 2 and a closer placement of the electrodes.

As shown in Figure 6c and Movie S1, Supporting Information, the butterfly can easily recover its PS (R_r = 95%) in a reasonably short time (<2 min), upon the application of the voltage.

Then, we investigated the possibility to drive a modular shape recovery by simply activating/deactivating time by time the power source.

For this purpose, a DLP-printed nanocomposite specimen (S0.5, 50 × 5 × 2 mm^3, copper electrodes placed at opposite ends of the longest side) was first programmed in a temporary bent configuration by using a U-shaped mold, as previously described (see Figure 5a). Then, the stepwise recovery of the PS was activated by turning on and off the voltage at different time intervals.

Figure 7 shows the modular recovery of the mentioned 3D-printed specimen as a function of time. First (A-point), the voltage is turned on and the recovery is activated via Joule heating. Then, after about 40 s, the power source is deactivated to stop the recovery (B-point, R_r = 27%). Nevertheless, an increase in the R_r was observed in the first 40 s after the voltage shutdown since the specimen requires a certain time to dissipate the Joule energy. But, as the specimen cools down, the recovery slows down reaching a plateau approximately after 80 s when the sample temperature becomes lower than its T_g (C-point, R_r = 47%). Remarkably, the shape remains almost unaltered for 100 s, demonstrating the high fixity of the new intermediate TS once the sample is cooled down, even in the absence of an external constraint. Finally, the voltage is turned on again (D-point) to complete the recovery of the PS in less than 2 min (E-point, R_r = 94%).

Finally, the selective shape memory capability of the DPL-printed nanocomposites was explored. To prove this, we prepared a zig-zag-shaped structure and we positioned four electrodes along it (**Figure 8**a). First, electrodes 1 and 4 were connected to the power source so that the whole specimen can be heated to above its T_g via Joule effect and manually straightened while in its rubbery state. The temporary linear configuration is fixed by rapid cooling at RT (Figure 8b). Then, two different strategies were followed to recover the PS (see Movie S2, Supporting Information). The first one (Figure 8c) relies on regaining the PS in one single stage (RS). Here, the PS was fully recovered (R_r = 96%) in less than 4 min, by simply reconnecting electrodes 1 and 4. The second strategy, instead, is based on a stepwise recovery (RSX, where X is the number of the recovery stage) achieved by connecting two adjacent electrodes at a time (electrodes 1–2, 2–3, and 3–4 for RS1, RS2, and RS3, respectively, Figure 8d). In such a way, it is possible to enable a selective Joule heating to trigger the shape recovery of one region of the sample at a time. As can be clearly observed in Figure 8d, each stage (RS1, RS2, and RS3) leads to the selective recovery of the region of the specimen enclosed between two connected electrodes without affecting the adjacent regions. However, a fourth stage is required to complete the recovery of the PS because, whilst the regions of the specimen covered by the electrodes 2 and 3 were heated and deformed when obtaining the TS, these regions were not heated during the selective recovery. This prevents the complete recovery of the PS since the internal stresses generated in the regions of the specimen close to such electrodes during the programming of the TS cannot be totally released. Therefore, a final recovery stage (RS4) was carried out by reconnecting the electrodes 1 and 4, so that the whole specimen is homogeneously reheated, resulting in a R_r increase from 88% to above 92%.

© 2021 The Authors. Advanced Functional Materials published by Wiley-VCH GmbH

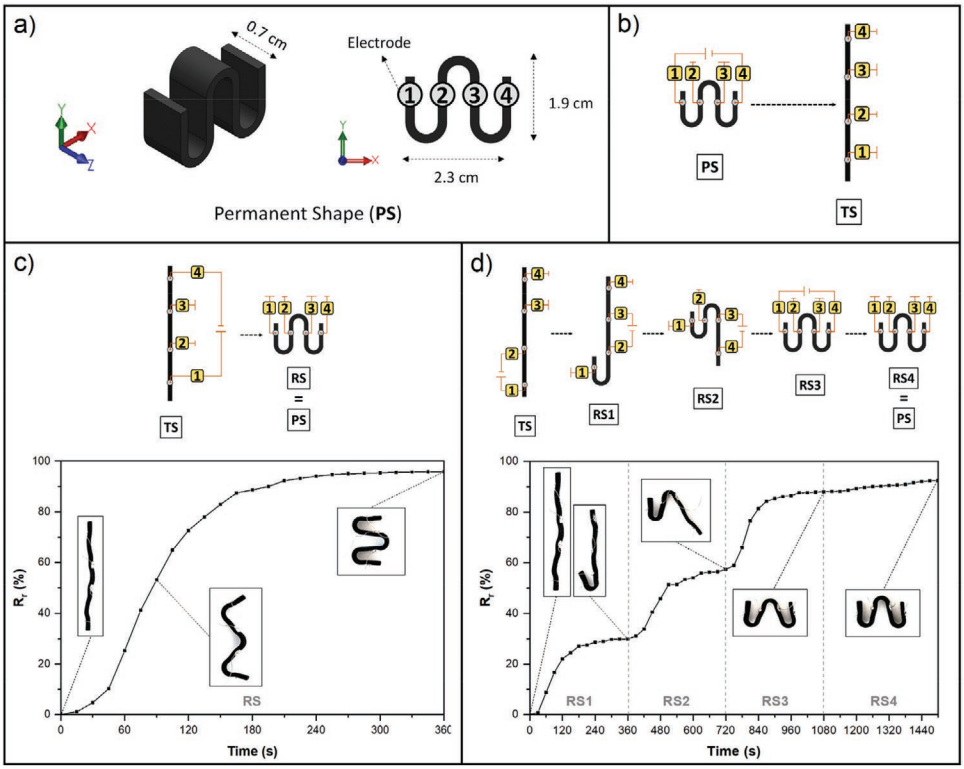


Figure 8. a) CAD model of the zig-zag shaped structure and positioning of the 4 electrodes to drive a selective shape recovery; b) programming of the temporary straightened shape (TS); c) recovery of the PS in one single stage (RS); and d) stepwise recovery of the PS (RS1, RS2, and RS3 achieved by connecting two adjacent electrodes at a time and RS4 reconnecting again electrodes 1–4).

3. Conclusions

In this work, photocurable and electro-activated SMPCs made of an amorphous thermosetting PEGDA-*co*-PHEMA matrix embedding CNTs were successfully prepared via DLP 3D-Printing. First, the thermomechanical properties of the polymeric matrix were tailored by finely tuning the PEGDA/HEMA ratio, aimed to prepare SMPs able to store a mechanically stable TS at room temperature, while CNTs were used to enable the electrical conductivity. The effect of the nanofiller onto the photopolymerization kinetics was evaluated, as well as its influence on the electrical properties of the printed structures. Then, the shape memory behavior of the DLP-printed nanocomposites was investigated exploiting the heat developed when applying a voltage (Joule heating). The high shape fixity and shape recovery ratios achieved (R_f = 100%, R_r > 95%), confirmed the significant electrically-triggered responsiveness of such nanocomposites, envisaging their potential integration in the fabrication of smart electroactive structures via 4D-Printing. Finally, the feasibility to drive a modular and selective recovery by Joule heating was successfully demonstrated.

4. Experimental Section

Materials: Poly(ethylene glycol) diacrylate (PEGDA, Mn = 700 g mol^{-1} and Mn = 250 g mol^{-1}), 2-hydroxyethyl methacrylate (HEMA, ≥99%, contains ≤50 ppm monomethyl ether hydroquinone as inhibitor), bis-(2,4,6-trimethylbenzoyl) phenylphosphine oxide (BAPO, registered trade name Omnicure 819, used as photoinitiator), and 2-(4-Dimethylaminophenylazo)benzoic acid (methyl red) were purchased from Sigma Aldrich and used as received. NC7000 Multi-walled CNTs (average length and diameter of 1.5 µm and 9.5 nm, respectively, good UV resistance) were supplied by Nanocyl.

Preparation and Characterization of the Photocurable Formulations: 3D-printable formulations were prepared as follows. First, CNTs were dispersed in HEMA sonicating for 30 min (LBS1, Falc Instrument; 50/60 Hz, 100 W), while BAPO photoinitiator was dissolved in PEGDA by magnetic stirring for 30 min. Then, the two solutions were merged and the mixture was homogenized by a high-shear dispersion process, using an Ultraturrax (IKA T10) for 5 min at 13 500 rpm.

Real-time photorheology was performed using an Anton PAAR Modular Compact Rheometer (Physica MCR 302, Graz, Austria) in parallel-plate mode (25 mm diameter), equipped with a UV-light source (Hamamatsu LC8 lamp, 40 mW cm^{-2}) underneath the bottom plate. The gap between the plates was set to 200 µm and the samples were kept in isothermal condition (25 °C) and under a constant shear angular frequency (10 rad s^{-1}). The measurements were carried out in the linear viscoelastic region (LVR) of the liquid formulations setting a strain amplitude of 1% (according to preliminary amplitude sweep tests). The photo-reactivity of the photocurable formulations was investigated by following the concomitant changes of both the storage and loss moduli (G′ and G″, respectively) during UV-light irradiation. The light was switched on after 60 s to let the system stabilize before the onset of polymerization. The delay time (i.e., the time required to induce crosslinking) and the curing rate (measured as the slope of the curve in the first 10 s of crosslinking) were also recorded. The measurements were repeated three times and the results were averaged.

Flow measurements were performed using the same rheometer to evaluate the rotational viscosity of the liquid formulations. The measurements were carried out at 25 °C, keeping the plate gap at 200 µm and varying the shear rate from 0.1 to 100 s^{-1}.

© 2021 The Authors. Advanced Functional Materials published by Wiley-VCH GmbH

3D-Printing of Nanocomposite SMPs and Material Characterization: An ASIGA UV-MAX X27 DLP printer (XY pixel resolution of 27 µm; building volume of $119 \times 67 \times 75$ mm^3; light source emitting at 385 nm) was used as 3D-printing equipment. 3D digital models having different geometries were prepared using Solidworks 2019 CAD software and converted in STL file formats. During printing, the layer thickness and the light intensity were fixed at 50 µm and 40 mW cm^{-2}, respectively, while the exposure time was tailored for each specific formulation. A post-curing process was performed on the printed specimens using a medium-pressure mercury lamp provided by Robot Factory (3 min, UV-light intensity 12 mW cm^{-2}).

3D-Scanning was performed to evaluate the fidelity of the built objects to the original CAD files, using a 3D optical scanner (E3, 3Shape). The scanned data and the reference model were aligned before being compared. The results of the comparative analysis were displayed as a colored 3D map displaying the geometrical deviation from the reference model.

GC measurements were performed to evaluate the insoluble fraction of the printed specimens (covalently crosslinked polymer). The samples were held in an ultra-fine metal net, weighed, and immersed in chloroform to remove the soluble fraction (un-crosslinked polymer). After 24 h, the samples were removed from the chloroform bath and dried in an oven (80 °C) until no mass variation was detected by gravimetric analysis. The GC was determined using the following Equation (1):

$$GC(\%) = \frac{m_{dried}}{m_0} \times 100 \quad (1)$$

where m_0 is the initial mass of the sample and m_{dried} is the residual mass after the solvent extraction. The measurements were repeated three times and the results were averaged.

Dynamic mechanical thermal analyses (DMTAs) were carried out on thin rectangular DLP-printed specimens ($10 \times 5 \times 1$ mm^3), using a Tritec 2000 DMA (Triton Technology Ltd, London UK). The measurements were conducted by setting a temperature ramp of 3 °C min^{-1}, applying a force to the sample with a frequency of 1 Hz, and with a displacement of 20 µm. The evolution of both the storage and loss moduli (E' and E'', respectively) during the temperature ramp was recorded. The glass transition temperature (T_g) was taken as the temperature corresponding to the peak of the damping factor (tan δ) curve, as recommended by conventions.

DC volume conductivity tests were carried out according to ASTM D257 standard by using a Keithley 237 High Voltage Source Measure Unit. The electrical resistance, R, was obtained from the V-I (voltage-intensity) slope, applying voltages in the 0–40 V range and the electrical conductivity was then obtained from the Equation (2), where L is the distance between the electrodes and A the cross-sectional area of the specimen.

$$\text{Electrical conductivity} = \frac{L}{A \times R} \quad (2)$$

The thermoelectrical behavior of the SMP nanocomposites ($30 \times 10 \times 2$ mm^3) was characterized by Joule heating tests in order to determine the voltage needed to reach the T_g, Here, the average temperature increment with regard to room temperature (ΔT_{av}) was recorded with an infrared thermo-camera FLIR E5 (IR resolution of 10 800 pixels, thermal sensibility of 0.1 °C between –20 and 250 °C) as a function of the applied voltage, in the range 0–300 V. Copper wire electrodes were placed onto the two opposite faces of the specimens (10×2 mm^2) with a silver conductive paste to reduce contact resistance.

The shape memory behavior was monitored by following two different strategies, based on the heating source used to increase the temperature of the samples to above their T_g. The printed nanocomposite specimens ($30 \times 10 \times 2$ mm^3) were heated at $T = T_g + 20$ °C either by direct heating, using a heating plate (AREX Digital Pro, VELP Scientifica), or via Joule heating. The shape memory properties of the undoped specimens thermally-activated via direct heating were taken as reference. A 3D-printed mold was used to fix at RT the temporarily deformed shape (bending angle of 180° and curvature radius of 3.25 mm), as shown in Figure S3, Supporting Information. Once the specimen reaches RT, it was removed from the mold and kept at RT for 5 min. Finally, it was heated again at $T = T_g + 20$ °C to recover the original shape. The shape memory efficiency was measured by monitoring the evolution of the bending angle over time by image analysis (ImageJ software). The shape fixity ratio (R_f) and shape recovery ratio (R_r) were obtained by using the following Equations (3) and (4), respectively.

$$R_f(\%) = \left(1 - \frac{\theta_S - \theta_F}{\theta_S}\right) \times 100 \quad (3)$$

$$R_r(\%) = \frac{\theta_F - \theta_R}{\theta_F} \times 100 \quad (4)$$

Here, θ_s represents the angle of the mold, θ_F the angle of the fixed shape, and θ_R the angle of the recovered shape measured using the ImageJ software.

Supporting Information

Supporting Information is available from the Wiley Online Library or from the author.

Acknowledgements

A.Cor. and A.Cos. contributed equally to this work. This work was supported by the Ministerio de Economía y Competitividad of Spanish Government [PID2019-106703RB-I00], Comunidad de Madrid regional government [ADITIMAT-CM, S2018/NMT-4411] and by Compagnia di San Paolo.

Open access funding provided by Politecnico di Torino within the CRUI-CARE Agreement.

Conflict of Interest

The authors declare no conflict of interest.

Data Availability Statement

Research data are not shared.

Keywords

4D printing, carbon nanotubes, digital light processing, electro-activated composites, shape memory polymer

Received: July 13, 2021
Revised: August 26, 2021
Published online:

[1] S. Tibbits, *Archit. Des.* **2014**, *84*, 116.
[2] B. Zhang, H. Li, J. Cheng, H. Ye, A. H. Sakhaei, C. Yuan, P. Rao, Y.-F. Zhang, Z. Chen, R. Wang, X. He, J. Liu, R. Xiao, S. Qu, Q. Ge, *Adv. Mater.* **2021**, *33*, 2101298.
[3] X. Kuang, D. J. Roach, J. Wu, C. M. Hamel, Z. Ding, T. Wang, M. L. Dunn, H. J. Qi, *Adv. Funct. Mater.* **2019**, *29*, 1805290.

© 2021 The Authors. Advanced Functional Materials published by Wiley-VCH GmbH

[4] H. Chu, W. Yang, L. Sun, S. Cai, R. Yang, W. Liang, H. Yu, L. Liu, *Micromachines* **2020**, *11*, 796.
[5] Y. Xia, Y. He, F. Zhang, Y. Liu, J. Leng, *Adv. Mater.* **2020**, *33*, 2000713.
[6] I. A. Rousseau, *Polym. Eng. Sci.* **2008**, *48*, 2075.
[7] A. S. Gladman, E. A. Matsumoto, R. G. Nuzzo, L. Mahadevan, J. A. Lewis, *Nat. Mater.* **2016**, *15*, 413.
[8] D. Raviv, W. Zhao, C. Mcknelly, A. Papadopoulou, A. Kadambi, B. Shi, S. Hirsch, D. Dikovsky, M. Zyracki, C. Olguin, R. Raskar, S. Tibbits, *Sci. Rep.* **2014**, *4*, 7422.
[9] H. Yang, W. R. Leow, T. Wang, J. Wang, J. Yu, K. He, D. Qi, C. Wan, X. Chen, *Adv. Mater.* **2017**, *29*, 1701627.
[10] M. Nadgorny, Z. Xiao, C. Chen, L. A. Connal, *ACS Appl. Mater. Interfaces* **2016**, *8*, 28946.
[11] M. Zarek, M. Layani, I. Cooperstein, E. Sachyani, D. Cohn, S. Magdassi, *Adv. Mater.* **2016**, *28*, 4449.
[12] M. Zarek, M. Layani, S. Eliazar, N. Mansour, I. Cooperstein, E. Shukrun, A. Szlar, D. Cohn, S. Magdassi, *Virtual Phys. Prototyping* **2016**, *11*, 263.
[13] Y. Mao, K. Yu, M. S. Isakov, J. Wu, M. L. Dunn, H. Jerry Qi, *Sci. Rep.* **2015**, *5*, 13616.
[14] M. Layani, X. Wang, S. Magdassi, *Adv. Mater.* **2018**, *30*, 1706344.
[15] C. L. Lewis, E. M. Dell, *J. Polym. Sci., Part B: Polym. Phys.* **2016**, *54*, 1340.
[16] X. Huang, M. Panahi-Sarmad, K. Dong, R. Li, T. Chen, X. Xiao, *Composites, Part A* **2021**, *147*, 106444.
[17] Y. Liu, F. Zhang, J. Leng, K. Fu, X. L. Lu, L. Wang, C. Cotton, B. Sun, B. Gu, T. W. Chou, *Adv. Mater. Technol.* **2019**, *4*, 1900600.
[18] W. S. Chow, Z. A. M. Ishak, *eXPRESS Polym. Lett.* **2020**, *14*, 416.
[19] T. Liu, T. Zhou, Y. Yao, F. Zhang, L. Liu, Y. Liu, J. Leng, *Composites, Part A* **2017**, *100*, 20.
[20] H. H. Le, I. Kolesov, Z. Ali, M. Uthardt, O. Osazuwa, S. Ilisch, H. J. Radusch, *J. Mater. Sci.* **2010**, *45*, 5851.
[21] L. H. Shao, B. Zhao, Q. Zhang, Y. Xing, K. Zhang, *Extreme Mech. Lett.* **2020**, *39*, 100793.
[22] J. M. Jani, M. Leary, A. Subic, M. A. Gibson, *Mater. Des.* **2014**, *56*, 1078.
[23] L. Sun, W. M. Huang, Z. Ding, Y. Zhao, C. C. Wang, H. Purnawali, C. Tang, *Mater. Des.* **2012**, *33*, 577.
[24] H. Lu, W. M. Huang, F. Liang, K. Yu, *Materials* **2013**, *6*, 3742.
[25] I. T. Garces, C. Ayranci, *Rapid Prototyp. J.* **2021**, *27*, 379.
[26] X. Wang, J. Sparkman, J. Gou, *Compos. Sci. Technol.* **2017**, *141*, 8.
[27] H. Wei, X. Cauchy, I. O. Navas, Y. Abderrafai, K. Chizari, U. Sundararaj, Y. Liu, J. Leng, D. Therriault, *ACS Appl. Mater. Interfaces* **2019**, *11*, 24523.
[28] F. Guo, X. Zheng, C. Liang, Y. Jiang, Z. Xu, Z. Jiao, Y. Liu, H. T. Wang, H. Sun, L. Ma, W. Gao, A. Greiner, S. Agarwal, C. Gao, *ACS Nano* **2019**, *13*, 5549.
[29] X. Wan, F. Zhang, Y. Liu, J. Leng, *Carbon* **2019**, *155*, 77.
[30] Q. Wang, X. Tian, L. Huang, D. Li, A. V. Malakhov, A. N. Polilov, *Mater. Des.* **2018**, *155*, 404.
[31] C. Yang, B. Wang, D. Li, X. Tian, *Virtual Phys. Prototyping* **2017**, *12*, 69.
[32] S. T. Ly, J. Y. Kim, *Int. J. Precis. Eng. Manuf. – Green Technol.* **2017**, *4*, 267.
[33] Q. Mu, L. Wang, C. K. Dunn, X. Kuang, F. Duan, Z. Zhang, J. H. Qi, T. Wang, *Addit. Manuf.* **2017**, *18*, 74.
[34] A. Cosola, M. Sangermano, D. Terenziani, R. Conti, M. Messori, H. Grützmacher, C. F. Pirri, A. Chiappone, *Appl. Mater. Today* **2021**, *23*, 101060.
[35] G. Liu, X. Ding, Y. Cao, Z. Zheng, Y. Peng, *Macromolecules* **2004**, *37*, 2228.
[36] B. S. Lee, B. C. Chun, Y. C. Chung, K. Il Sul, J. W. Cho, *Macromolecules* **2001**, *34*, 6431.
[37] Y. Liu, C. Han, H. Tan, X. Du, *Mater. Sci. Eng., A* **2010**, *527*, 2510.
[38] C. L. Lewis, K. Stewart, M. Anthamatten, *Macromolecules* **2014**, *47*, 729.
[39] S. W. Kuo, H. T. Tsai, *Macromolecules* **2009**, *42*, 4701.
[40] L. Song, W. Hu, G. Wang, G. Niu, H. Zhang, H. Cao, K. Wang, H. Yang, S. Zhu, *Macromol. Biosci.* **2010**, *10*, 1194.
[41] H. Koerner, R. J. Strong, M. L. Smith, D. H. Wang, L. S. Tan, K. M. Lee, T. J. White, R. A. Vaia, *Polymer* **2013**, *54*, 391.
[42] X. L. Wu, S. F. Kang, X. J. Xu, F. Xiao, X. L. Ge, *J. Appl. Polym. Sci.* **2014**, *131*, 40559.
[43] S. Miao, H. Cui, T. Esworthy, B. Mahadik, S. Lee, X. Zhou, S. Y. Hann, J. P. Fisher, L. G. Zhang, *Adv. Sci.* **2020**, *7*, 1902403.
[44] G. Gonzalez, A. Chiappone, I. Roppolo, E. Fantino, V. Bertana, F. Perrucci, L. Scaltrito, F. Pirri, M. Sangermano, *Polymer* **2017**, *109*, 246.
[45] L. Pezzana, G. Riccucci, S. Spriano, D. Battegazzore, M. Sangermano, A. Chiappone, *Nanomaterials* **2021**, *11*, 373.
[46] M. Sangermano, S. Pegel, P. Pötschke, B. Voit, *Macromol. Rapid Commun.* **2008**, *29*, 396.
[47] A. Chiappone, E. Fantino, I. Roppolo, M. Lorusso, D. Manfredi, P. Fino, C. F. Pirri, F. Calignano, *ACS Appl. Mater. Interfaces* **2016**, *8*, 5627.
[48] E. Fantino, A. Chiappone, I. Roppolo, D. Manfredi, R. Bongiovanni, C. F. Pirri, F. Calignano, *Adv. Mater.* **2016**, *16*, 3712.
[49] X. Li, H. Gao, W. A. Scrivens, D. Fei, X. Xu, M. A. Sutton, A. P. Reynolds, M. L. Myrick, *Nanotechnology* **2004**, *15*, 1416.
[50] J. N. Coleman, S. Curran, A. B. Dalton, A. P. Davey, B. Mccarthy, W. Blau, R. C. Barklie, *Phys. Rev. B* **1998**, *58*, R7492.
[51] D. Ponnamma, N. Ninan, S. Thomas, in *Applications of Nanomaterials: Advances and Key Technologies* (Eds.: S. M. Bhagyaraj, O. S. Oluwafemi, N. Kalarikkal, S. Thomas), Elsevier Ltd, Amsterdam, Netherlands **2018**, p. 391.
[52] A. Jiménez-Suárez, J. Martín-González, X. F. Sánchez-Romate, S. G. Prolongo, *Compos. Sci. Technol.* **2020**, *199*, 108321.
[53] W. Jian, X. Wang, H. Lu, D. Lau, *Compos. Sci. Technol.* **2021**, *211*, 108849.
[54] S. H. Jang, D. Kim, Y. L. Park, *Materials* **2018**, *11*, 1775.
[55] T. Ragab, C. Basaran, *J. Appl. Phys.* **2009**, *106*, 063705.
[56] P. Gautreau, T. Ragab, C. Basaran, *J. Appl. Phys.* **2012**, *112*, 103527.

© 2021 The Authors. Advanced Functional Materials published by Wiley-VCH GmbH